Cement and Concrete Research 193 (2025) 107873

Contents lists available at ScienceDirect

Cement and Concrete Research

journal homepage: www.elsevier.com/locate/cemconres

Comparative study of the early stages of crystallization of calcium silicate hydrate (C-S-H) and calcium aluminate silicate hydrate (C-A-S-H)

Yannick H. Emminger, Luca Ladner, Cristina Ruiz-Agudo *

Physical Chemistry, University of Konstanz, Universitätsstrasse 10, D-78457 Konstanz, Germany

ARTICLE INFO

Keywords:
Cement hydrates
C-S-H
C-A-S-H
Nucleation
Non-classical crystallization

ABSTRACT

The use of SCMs as partial substitutes for PC has made C-A-S-H a key binding phase in modern cement, yet its crystallization mechanism remains elusive. This study investigates the early stages of synthetic C-A-S-H formation and compares them with C-S-H using double addition of stoichiometric calcium and silicon amounts at a Ca/Al ratio of 5. Through real-time monitoring of solution parameters—transmittance, free Ca^{2+} conductivity, and pH—complemented by structural and morphological characterization (FTIR, XRD, SEM, TEM, and NMR), we demonstrate that C-A-S-H formation is at least a two-step process involving amorphous globules, which then evolve into foil-like particles with higher crystallinity. Additionally, we reveal that Al promotes Ca binding during the prenucleation stage and slightly accelerates nucleation. These results highlight important differences in the formation pathways of both hydrates, particularly the extended stability of the C-A-S-H globules, which might affect the workability and setting time in aluminium-containing blended cements.

1. Introduction

From a materials perspective, the most straightforward method to enhance the environmental performance of the construction industry is to substitute a portion of the Portland cement (PC) with supplementary cementitious materials (SCMs) [1], as endorsed by the United Nations Environment Program for Sustainable Building and Climate Initiative (UNEP-SBCI) [2]. Nevertheless, the cement hydrates formed in the presence of SCMs, typically characterized by a lower calcium content, exhibit notable differences compared to those resulting from the hydration of PC alone. Most SCMs introduce additional aluminium and silicon during the hydration process [3], resulting in alterations in the C-S-H phase compared to that formed in plain PC [4]. These differences impact the paste's volume, porosity, and microstructure, affecting the material's strength and durability [5].

The rise in SCM usage has made calcium aluminate silicate hydrate (C-A-S-H) the primary phase in blended cements. This Al-modified hydrate differs from traditional C-S-H, which have led to extensive research efforts aimed at understanding the properties of the C-A-S-H phase, given its importance. While state of the art research using ^{27}Al NMR spectroscopy and computer simulations has revealed fundamental molecular-level insights about aluminium incorporation in C-A-S-H—including the increase in mean chain length (MCL) [6–8], aluminium coordination environment [9–11], and the cross-linking of adjacent aluminosilicate chains in low-calcium gels [12]—our understanding of early-stage C-A-S-H crystallization remains limited compared to that of C-S-H. C-S-H formation has been demonstrated to proceed through distinct stages — including prenucleation clusters [13] and amorphous liquid-like [13] and solid-like [14–17] precursors — before evolving into sheet-like structures. However, the role of aluminium in altering this crystallization pathway, as well as whether C-A-S-H follows similar formation mechanisms, remains unclear. Gaining insights into the formation mechanisms of C-A-S-H could contribute to accelerate its formation of C-A-S-H in less reactive systems, ultimately reducing their setting time.

This study aims to gain deeper insights into the nucleation of C-A-S-H by directly comparing it with the C-S-H formation process under identical synthetic conditions. To achieve this, we monitored key physicochemical parameters of the reaction media—transmittance, free Ca^{2+} conductivity, and pH—complemented by structural and morphological characterization (FTIR, XRD, SEM, TEM, and NMR) during the synthetic formation of both C-S-H and C-A-S-H. The different probes provide us with highly valuable information about the free and bound ions in solution and the distinct stages present in the crystallization process of both phases. Furthermore, this simplified and controlled system offers a reproducible crystallization scenario, enabling a consistent investigation

* Corresponding author.
E-mail address: cristina.ruiz-agudo@uni-konstanz.de (C. Ruiz-Agudo).

https://doi.org/10.1016/j.cemconres.2025.107873
Received 21 August 2024; Received in revised form 7 March 2025; Accepted 10 March 2025
Available online 13 March 2025

of the early stages of the process and modifications introduced by foreign ions [18] and molecules [19]. By comparing C-S-H and C-A-S-H under identical experimental conditions, we have gained direct insights into the influence of aluminium on the early stages of the crystallization pathway of the primary hydrate and its effects on the resulting material's characteristics and microstructure.

2. Experimental section

2.1. Reagents

All the chemicals were used without any further purification. The sodium meta silicate (nonahydrate) $Na_2SiO_3 \cdot 9\ H_2O$ was provided by Acros Organics (CAS: 13517-24-3) and was used for preparing the 40 mM silicate solution. 1 M $CaCl_2$ stock solution from VWR Chemicals was used (CAS: 10043-52-4) and diluted with Milli-Q water to prepare the 40 mM calcium solution for the experiments. The aluminium chloride hexahydrate $AlCl_3 \cdot 6\ H_2O$ was purchased from Carl Roth GmbH & Co. KG (CAS: 7784-13-6). For the ethanol a p.a. solution from VWR Chemicals (CAS: 64-17-5) was used.

2.2. Titration setup

The titration apparatus is a compilation of various equipment manufactured by Metrohm AG. Titrandos 901 are used to add the stock solutions, which send the dosage information to Dosinos 800, from which the stock solutions are added from 2 mL burettes to the reaction vessel. The pH electrode (flat membrane electrode 6.0256.100), the Transmittance Optrode with a laser at 640 nm (Optrode 6.1115.000) and the Calcium ion selective electrode (ISE) (separated polymer membrane electrode 6.0508.110) are also controlled by the Titrandos. A conductivity module 856 measures the conductivity of the solution (5-ring conductivity cell 2.856.0210). A Teflon cup is the reaction vessel attached to a magnetic stirrer. The setup was located in a temperature-controlled room to counteract temperature fluctuations. All the titration methods are programmed with the software TiAmo™, where all the data is collected.

2.3. Calibration of electrodes

The Calcium ISE was calibrated to directly measure the free calcium concentration in the solution. A 40 mM $CaCl_2$ solution was prepared and added to 100 mL of Milli-Q water with a pH of 12 at a 0.1 mL/min rate. The transmittance, conductivity, pH value, and calcium potential were measured during the experiments. First, with the obtained data of the calcium potential and the respective concentration of calcium ions in the solution, an average Nernst equation was obtained (Eq. (1)):

$$E = \alpha + \beta \cdot ln(c) \quad (1)$$

The amount of free calcium ions in the reaction solution was calculated with these alpha and beta values. Due to material wear, four calibration curves were measured for one week, and the mean of the obtained alpha and beta were used to calculate the free amount of calcium ions. To ensure a precise measurement of the pH value, the electrode was calibrated once a week using standard buffers of pH 4.01, 7.00, and 9.00 by Metrohm. The cell constant of the conductivity electrode was determined with a 100 µS/cm conductivity standard solution from Metrohm. The Optrode does not require any calibration.

2.4. Synthesis of C-S-H and C-A-S-H

The C-S-H and C-A-S-H were synthesized using the above-mentioned double titration setup. For the synthesis of C-S-H, 30 mL of a solution containing 40 mM $CaCl_2$ and 30 mL of a solution containing 40 mM Na_2SiO_3 were titrated simultaneously to 100 mL Milli-Q water with a pH of 12 at a rate of 0.1 mL/min. The pH of the Milli-Q water was adjusted by titrating a 1 M NaOH solution to Milli-Q water while monitoring the pH. The reactants were added after 18000 s (5 h). 8 mM $AlCl_3$ was added to the $CaCl_2$ solution to synthesize C-A-S-H. The conductivity, pH, transmittance, and calcium potential were monitored during the experiments. Four replicas were conducted per experimental series. The solids were isolated by filtering the resulting dispersions through a 0.22 µm filter (Durapore Membrane Filter 0.22 µm), washed with 300 mL Milli-Q water, and dried in a vacuum cabinet at 40 °C. After drying, the precipitates were crushed and stored in a sealed snap-lid glass for further ex-situ analysis.

2.5. Aliquots-TEM-experiments

Separate titrations were carried out for the TEM investigations of the intermediate steps during the formation of both C-S-H and C-A-S-H. At different time periods, 200 µL of the reaction solution was removed with a pipette and quenched in 3 mL of ethanol. This ethanol solution was then drop-cast onto a TEM grid (Carbon Support Films on Cu 400 mesh grids, Quantifoil Micro Tools GmbH) and allowed to dry.

2.6. Powder X-ray diffraction (PXRD)

A Bruker AXS D8 Advance diffractometer in Bragg-Brentano configuration was used for the powder X-ray diffraction. The X-ray source provided Cu-K_α radiation of $\lambda = 1.542$ Å. The samples were scanned in the $5° < 2\theta > 70°$ range by a LynxEye detector.

2.7. Fourier-transformed infrared (FTIR) spectroscopy

FTIR spectra were measured by a Cary 630 FTIR Spectrometer from Agilent© Technologies Inc., covering a spectral range of 600–4000 cm^{-1}. It was measured in transmittance mode with 125 scans per step and a scan resolution of $<2\ cm^{-1}$. The measurement was recorded with the corresponding MicroLab software from Agilent©.

2.8. Magic angle solid state nuclear magnetic resonance (NMR)

The NMR measurements were performed using a Bruker Avance III 400WB (9.40 T) spectrometer equipped with a "PH MAS DVT 400W1 BL4 N-P/H" probe head. The measurements were conducted at a frequency of 104.26 MHz for ^{27}Al and 79.49 MHz for ^{29}Si, using a 4 mm Bruker CPMAS probe at a spinning frequency of 10 kHz.

For the ^{27}Al NMR measurements, the following parameters were applied: a high-power decoupling (hpdec) pulse program, 1024 scans, a time domain (td) of 6218 points, and a spectral width of 2997.27 ppm. The recycle delay (d1) was set to 0.1 s, the 90° pulse length (p1) was 3.9 µs, and the power level for excitation (plw1) was 86.5 W. The transmitter frequency offset (o1p) was adjusted to 0 ppm.

For the ^{29}Si NMR measurements, a cross-polarization (cp) pulse program was utilized, with 20480 scans, a time domain (td) of 3012 points, and a spectral width of 403.19 ppm. The recycle delay (d1) was 5 s, and the contact time (p15) for cross-polarization was set to 5 ms. The 90° pulse length (p3) was 2.4 µs, with a power level for excitation (plw1) of 100 W. The transmitter frequency offset (o1p) was also adjusted to 0 ppm.

2.9. Thermogravimetric analysis (TGA)

Thermogravimetric analysis (TGA) was performed by weighing 10–20 mg of sample powder into an Al_2O_3 crucible and then steadily heating it at a rate of 10 K/min up to 1213 K under nitrogen atmosphere in a Netzsch STA449 F3 Jupiter.

2.10. Scanning electron microscopy (SEM)

A scanning electron microscope (SEM) was used to analyse the

morphology of the final precipitates. A Zeiss Gemini 500 electron microscope (Carl Zeiss GmbH, Oberkochen, Germany) was utilized. The samples were put on a carbon tape and measured with an electron beam of 3 kV without prior sputtering at a working distance of 5 mm. For the elemental analysis by energy dispersive X-ray spectroscopy (EDX), an acceleration voltage of 9 kV and a working distance of 8.5 mm was used. For each system, the mean Ca/Si ratios were calculated from individual elemental analyses of 90–120 measurements. The data was analysed using the AZtech software from Oxford Instruments.

3. Results and discussion

3.1. Real-time evolution of the crystallization media

The investigation of calcium silicate hydrate (C-S-H) and calcium aluminate silicate hydrate (C-A-S-H) precipitation was conducted through titration experiments. This methodology generates supersaturation at a slow rate with respect to C-S-H and C-A-S-H, respectively, by adding the reactants to the reaction vessel stepwise. This experimental approach provides a highly reproducible crystallization scenario that enables a detailed investigation of the early stages of crystallization, from the initial prenucleation phase to the eventual formation of the solid phase [20]. Numerous authors have utilized it to obtain precise qualitative and quantitative data on the formation of several mineral phases [18,21], including C-S-H [22]. In this study, the evolution of various physicochemical parameters—including transmittance, conductivity, and free Ca^{2+} concentration—was monitored to identify the distinct stages of the crystallization process for both cement hydrates. All ex-situ analysis employed confirmed the formation of both phases using our methodology.

3.1.1. Transmittance

The Optrode probe's sensitivity to slight disruptions in the detected light beam, caused by the scattering of formed particles, makes transmittance monitoring a direct and effective approach to evaluate in situ C-S-H and C-A-S-H precipitation in liquid media. At the beginning of the experiments, the transmittance curve exhibited a plateau marked by maximum values, signifying a clear solution without any particles. Upon nucleation, a distinct decrease in the transmittance curve was observed (i.e., an increase in the turbidity in the solution/dispersion) due to the scattering of the light by the newly formed C-S-H/C-A-S-H particles. For the C-S-H experiments (blue line in Fig. 1a), this notable change on the transmittance curve occurs at approximately 3100 s (Fig. 1a), translating to an added calcium concentration of 1.8 mM. From this point, the transmittance decreased following a seemingly negative exponential decay function.

In contrast, the transmittance evolution observed for the C-A-S-H system (depicted by the orange line in Fig. 1a) revealed a distinctive two-step process. The initial drop in transmittance in the C-A-S-H system occurred at 2800 s (1.65 mM calcium), slightly earlier than in the C-S-H case. Unlike the behaviour in C-S-H, the transmittance curve for C-A-S-H exhibited two distinguishable regimes. The first regime can be described as linear, characterized by a notably slower decrease in the transmittance of the solution. This could be due to the different characteristics of the formed phase in this regime, such as size and water content, or simply to the presence of fewer particles. Around 7400 s (3.87 mM calcium), there was a sharp and sudden change in the transmittance of the solution, which we refer to as ‘kink’, which marks the transition from a linear decrease to an exponential decay. This hints at the presence of two distinct processes occurring during the formation of C-A-S-H, each affecting the transmittance of the solution differently.

3.1.2. Free Ca^{2+}

The evolution of the free-Ca^{2+} in solution measured with the Ca-ISE also revealed distinct regimes for each system (Fig. 2). In the prenucleation stage (regime I), i.e., before the transmittance drop, the free-Ca^{2+} rose linearly for both systems, reflecting the expected increase in the concentration of calcium ions in the solution due to the addition of $CaCl_2$ (Fig. 1b). The added amount of calcium is indicated by the dashed line (Fig. 1b). In the case of the C-S-H, the free-Ca^{2+} curve showed that most of the calcium added is free in solution, similarly to what was observed by Picker et al. [22], whereas for the case of C-A-S-H, a slightly lower slope in the ascending of the free-Ca^{2+} was observed. This suggests that Al promotes calcium binding in the prenucleation regime, most likely on calcium-silicate, calcium-aluminate, or calcium-silicate-aluminate species. The extensive formation of calcium-aluminate species was ruled out since no noticeable difference between the free-Ca^{2+} in the solution was observed by the addition of a $CaCl_2$ (40 mM) and $CaCl_2 + AlCl_3$ (40 mM and 8 mM) solution to a pH 12 solution (Fig. SI-1). Thus, this lower slope might be caused by a synergistic effect of the silicate and aluminate regarding calcium binding. Our group is currently investigating the differences in the ion associates present in solution before C-S-H and C-A-S-H nucleation using analytical ultracentrifugation (AUC).

In the case of the C-S-H system, the nucleation event based on the onset on the free-Ca^{2+} curve occurred at approximately 3300 s, which agreed with the drop in the transmittance curve. Following (regime II), a decrease in the free-Ca^{2+} was observed, caused by the consumption of calcium ions in the formation of C-S-H. Following this stage, the free-Ca^{2+} entered a semi-plateau region, remaining nearly constant until the end of the experiments (regime III). This suggests that, within regime III, the consumption of calcium ions is reduced compared to regime II. Thermodynamic calculations of the solution using PHREEQC with the database CEM 18 [23] showed that at the nucleation point (3300 s), supersaturation with respect to different C-S-H phases and tobermorite is reached (Fig. SI-2). However, the ex-situ analysis (see below) confirmed the exclusive formation of C-S-H. This phase, formed under our experimental conditions, is characterized by a Ca/Si ratio of

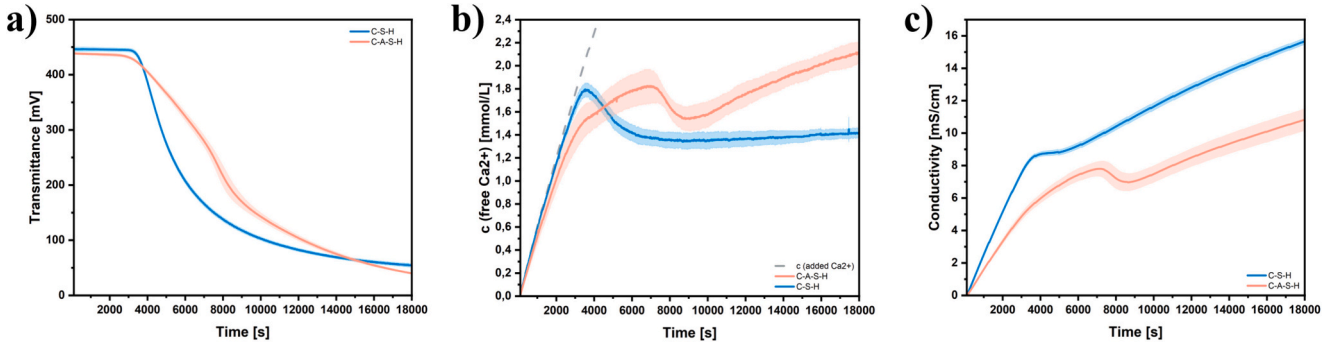

Fig. 1. Comparison of the a) transmittance, b) conductivity and c) concentration of free calcium ions in solutions of C-S-H in blue and C-A-S-H in orange with their respective standard deviation. (For interpretation of the references to colour in this figure legend, the reader is referred to the web version of this article.)

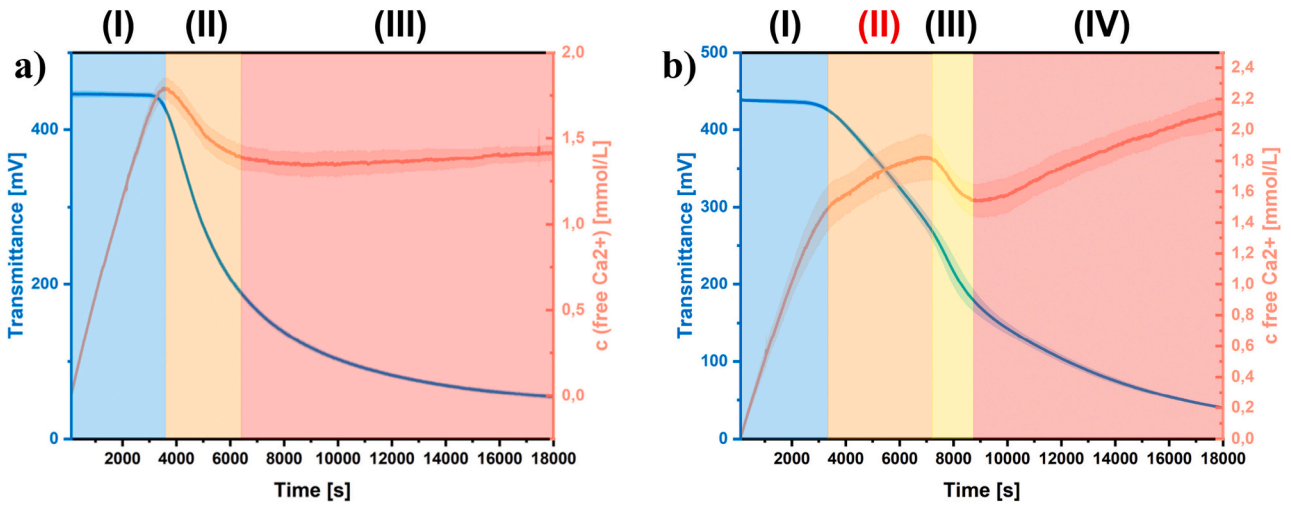

Fig. 2. Overlay of the transmittance measurements and free-Ca^{2+} concentration during the formation of a) C-S-H and b) C-A-S-H. For C-S-H, three distinct regimes can be identified based on the evolution of free-Ca^{2+} and transmittance. (I) initial stage with rising free-Ca^{2+} concentration and stable transmittance, (II) decreasing free-Ca^{2+} concentration and transmittance, and (III) final stage characterized by a stabilized free-Ca^{2+} concentration and further transmittance decrease. In the case of C-A-S-H, four regimes can be distinguished: (I) initial stage with rising free-Ca^{2+} concentration and stable transmittance, (II) intermediate phase with a noticeable lower slope in free-Ca^{2+} compared to (I) and linear decrease in the transmittance, (III) decrease in free-Ca^{2+} concentration and kink in the transmittance, and (IV) final stage with rising free-Ca^{2+} concentration and exponential decay in the transmittance.

approximately 1.1, which is closest to the CSH3T-T5C ($(CaO)_1(SiO_2)_1(H_2O)_2$) phase in the PHREEQC thermodynamic calculations (Fig. SI-2). The underlying reactions for the solubility products and parameters used for the thermodynamic calculations are listed in Table SI-1.

The free-Ca^{2+} curve for C-A-S-H showed a distinct behaviour (Fig. 1b). Around 3100 s, no decrease was noted in the free-Ca^{2+} curve, but a significant bending occurred. This inflection in the free-Ca^{2+} coincided with the earlier-mentioned drop in the transmittance for the C-A-S-H system (regime II in Fig. 2b). After approximately 7400 s, a maximum in the free-Ca^{2+} curve is reached, aligning with the kink observed in the transmittance curve. Afterward (regime III), the system behaved akin to C-S-H, initially displaying a decline in the calcium concentration followed by an ascent in the free-Ca^{2+} curve (regime IV) until the end of the addition (18000 s). The slope of the free-Ca^{2+} curve in this last regime was considerably steeper than in the case of the C-S-H system, reflecting a lower consumption of calcium ions in this regime in the presence of aluminium (Fig. 2b). This is most likely due to the lower Ca/Si ratios of approximately 0.91 in C-A-S-H precipitates. Moreover, the slope of the curve here is almost the same as for regime II, suggesting that the Ca-consumption is similar in both regimes.

3.1.3. Conductivity analysis

The conductivity curve is characterized by a linear increase from the beginning, attributed to the rise in free ions in the solution due to adding the reactants (Fig. 1c), as the free-Ca^{2+} curve showed. For the C-S-H, at approximately 3300 s, the conductivity curve displayed a saddle point and entered a semi-plateau regime where the value stays almost constant for 1600 s. A semi-plateau in the conductivity values indicates a significant decrease in the concentration of free ions in the solution compared to the prenucleation phase. At this stage, there is a balance between the conductivity contributed by the ions added to the medium and the decrease in conductivity caused by the ions being consumed in the formation of C-S-H. This point in the conductivity curve can be interpreted as the nucleation event, as it coincided with the drop in transmittance and the maximum in the free-Ca^{2+}. Following this semi-plateau, the conductivity increased further but with a reduced slope compared to the prenucleation regime, indicating the consumption of ions along this process but at a slower rate than the plateau phase, as the free Ca^{2+} curve also showed.

The conductivity curve for the C-A-S-H system exhibited different characteristics. In the prenucleation regime I, a linear increase in the conductivity was also observed up to 3100 s, albeit at a slower rate (i.e., lower slope) than for the C-S-H system. This was unexpected, as a steeper slope was anticipated due to adding extra Al^{3+} and Cl^- ions, which should have resulted in higher conductivity values. This indicates that more ions are bounded in the case of C-A-S-H compared to C-S-H in the prenucleation regime I, which also agrees with the increase in the Ca-bound in the presence of Al described earlier. In regime II, the conductivity curve presented a kink around 3000 s, reducing its slope significantly compared to the pre-nucleation regime. This indicates a greater number of ions bound in regime II than in regime I, which aligns perfectly with the observed change in the slope of the free Ca^{2+} curve. Approximately 7000 s after the beginning of the experiment, a relative maximum in the conductivity curve was reached, followed by a subsequent decline, which matched the results obtained for free-Ca^{2+} ions. Upon reaching a relative minimum, the conductivity increased again, exhibiting a slope similar to that observed in regime II.

This consistent behaviour across different measurements highlights notable differences in the early stages of C-S-H and C-A-S-H formation. The ‘kinks’ in all data sets might be key transition points related to an intermediate precursor phase during C-A-S-H formation, suggesting a more complex crystallization mechanism than C-S-H under our experimental conditions. The identification of an extra regime in the case of C-A-S-H (Fig. 2), where calcium (free-Ca^{2+} data) and most likely silicate and aluminate are bound (conductivity data), hints at the existence of a precursor phase to the final C-A-S-H phase. Considering these findings, ex-situ analyses were conducted to complement the solution's physicochemical analysis and elucidate the potential existence of any precursor phase in the C-A-S-H phase.

3.1.4. TEM analysis

TEM was used to gain deeper insights into the distinct regimes previously identified during the titration experiments for both C-S-H and C-A-S-H. To this end, aliquots were taken at different times shortly before nucleation and in the post-nucleation regime to compare the evolution of the precipitates in the Al-containing and Al-free systems. For the C-S-H system, soon after the nucleation point (4000 s), the TEM analysis showed already the presence of C-S-H foils with a poorly crystalline character (Fig. 3a). Aliquots taken at longer times (6000 s, 13000 s, and

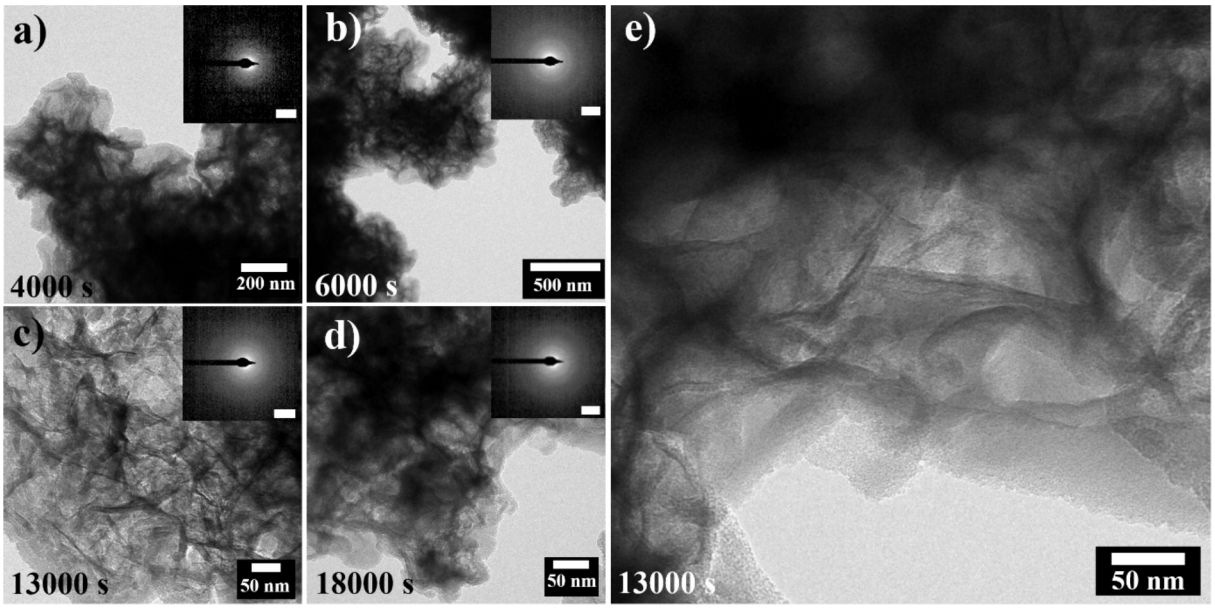

Fig. 3. TEM images of the C-S-H sheets taken from aliquots after 4000 s, 6000 s, 13000 s and 18000 s, each with their corresponding SAED as an inset in the respective image. Scale of the SAED: 5 nm^{-1}.

18000 s) also showed only the presence of C-S-H foil-like structures (Fig. 3b, c, d).

In contrast to Schönlein et al. [17] and Krautwurst et al. [14], our study of C-S-H formation did not reveal a transition from globules to foils; instead, only foil structures were observed. This discrepancy may be attributed to differences in synthesis methods. Schönlein et al. directly mixed solutions at pH 12.5 and allowed them to react for various durations before quenching, examining systems with and without polycarboxylates (PCEs). Their results showed that PCEs stabilized globules for several hours, while in PCEs-free systems, globules appeared very early in experiments. Krautwurst et al., on the other hand, rapidly added sodium metasilicate to a near-saturated $Ca(OH)_2$ solution at pH 12.86. These observations were later explained by Shen et al., who demonstrated that the two-step formation process of C-S-H is pH dependent, occurring at pH values between 12.35 and 13.00 and becoming more pronounced at higher pH [15]. In this range, the researchers observed an amorphous precursor undergoing a transformation into a foil-like C-S-H phase, which was subsequently confirmed in a separate study conducted at pH 12.6 [16]. In this latter study, the researchers identified a globular, metastable amorphous intermediate that underwent a transformation via non-classical nucleation [16]. This pH dependence not only explains the observations in Krautwurst's study [14] but is also particularly relevant to our work, as we operate below this pH threshold.

It was observed that the foils tend to develop sharper and more defined edges at longer times (Fig. 3e). The selected area electron diffraction (SAED) analyses showed in all aliquots, the material is poorly crystalline, confirmed by broad rings with an estimated d-spacing of approximately 3.00 Å (Fig. 3a inset), corresponding to the C-S-H (110) plane as shown by Kanchanason et al. [24]. In addition, in some regions, the estimated d-spacings matched with 2.8 Å (200) and 1.8 Å (020). Regarding the composition, EDX analysis showed that Ca and Si are homogeneously distributed in the sample (Fig. SI-3) and that Na is slightly incorporated in the material, as it was reported by Krautwurst et al. [14]. These compositional analyses were used only qualitatively since the EDX conducted in the SEM on the final material is more representative of the overall composition. In contrast to Krautwurst, we did not detect C-S-H globules in any of the C-S-H samples. While it does not rule out their existence, it does suggest a relatively short lifetime of this precursor phase under our experimental conditions.

In the case of the C-A-S-H aliquots taken at 5000 s (Fig. 4a) and 7000 s (Fig. 4b, c, d), drawn from the media before the kink in the transmittance and the onset on the free-Ca^{2+}, the TEM analysis revealed the presence of large agglomerates composed by globular nanoparticles. According to the SAED patterns, these structures were characterized by a lower crystallinity than the C-S-H samples. The SAED rings are broader than in the absence of Al, making the assignment of a d-spacing not possible (inset in Fig. 4a and b). To further characterize these early-stage structures, we are employing AUC, which has previously revealed the presence of liquid-like entities of similar sizes to the C-A-S-H globules during C_3S hydration [13]. Our ongoing AUC investigations aim to track the size, density, and temporal evolution of these precursor entities, thereby providing deeper insights into the way aluminium influences the formation process.

In the sample 7000 s, the globules formed part of networks connected by thinner regions (Fig. 4b) or agglomerated (Fig. 4c). Higher magnification images showed their nanometre sizes and ill-defined morphologies (Fig. 4d). EDX elemental maps showed that Ca, Al, and Si were homogeneously distributed on the structures (Fig. 5). The elevated pH conditions (pH 12) during synthesis promote minimal sodium incorporation into the structure. This incorporation mechanism can be attributed to the deprotonation of surface silanol groups ($\equiv$Si-OH $\rightarrow$ $\equiv$Si-O^-) at high pH values, which subsequently enhances the alkali binding capacity of both calcium-silicate-hydrate (C-S-H) and calcium-aluminium-silicate-hydrate (C-A-S-H) phases [25,26].

C-A-S-H aliquots taken at 9000 s showed foil-like structures for the first time (Fig. 6a), together with globules (Fig. 6b). In the aliquot taken at 14000 s, most of the sample was composed of foil-like structures (Fig. 6c), but still, some globules were observed at this time. The EDX analysis of the foils at 14000 s showed that in the same way as in the globules, Ca, Si, and Al are evenly distributed across the material (Fig. SI-4). The SAED of the C-A-S-H foils appeared more defined than for the globules; however, it is still broader than for C-S-H, making the assignment of the d-spacings not possible.

TEM analysis supports the proposed two-step process in the formation of C-A-S-H in conjunction with transmittance measurements, free-Ca^{2+} concentration, and conductivity evolution. By employing cryo-TEM, Tang et al. were able to elucidate a non-classical nucleation process underlying the formation of aluminosilicate gels from metakaolin. This process is characterized by a series of distinct transitional stages,

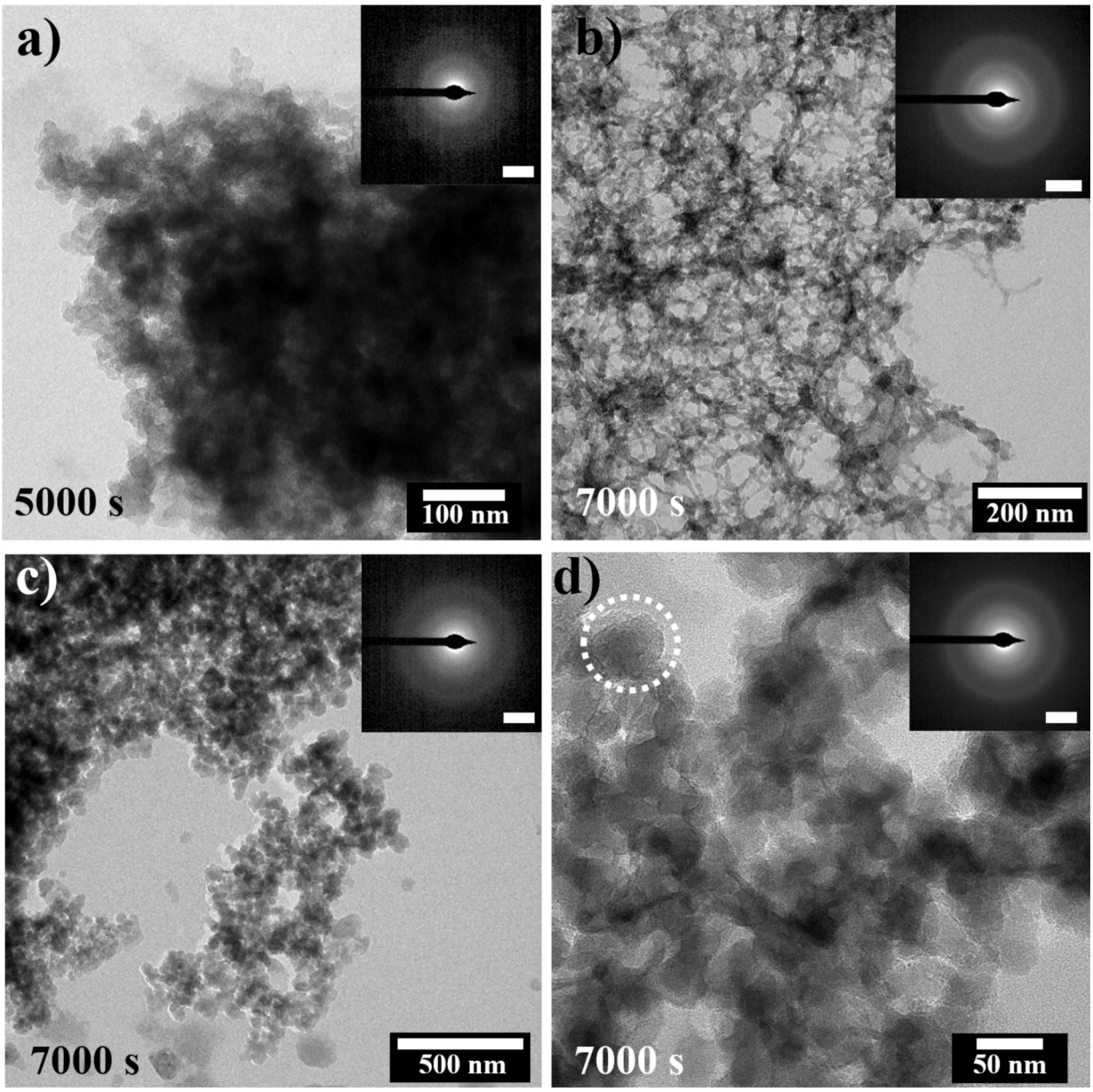

Fig. 4. TEM images of the C-A-S-H samples taken from aliquots after 5000 s and 7000 s, each with their corresponding SAED as an inset in the respective image. Scale of the SAED: 5 nm^{-1}.

including the formation of prenucleation clusters (1–2 nm), aggregated clusters, and finally, the development of N-A-S-H gels, which is followed by a final reorganization step [27]. Our study was limited to the direct observation of only two steps in C-A-S-H formation. However, Sowoidnich et al. had previously demonstrated the existence of prenucleation clusters in C-S-H systems [13], which led us to hypothesise that similar species form during C-A-S-H formation. The conductivity and free-Ca^{2+} measurements indicate the presence of ion associates in solution before nucleation, but their size and composition remain unknown and require the use of analytical techniques like AUC or cryo-TEM for characterization.

The observed two-step process involves the initial formation of C-A-S-H globules and their subsequent transformation into foil-like structures, revealing distinct differences between C-S-H and C-A-S-H formation pathways, particularly in the extended stability of the C-A-S-H globules. De Matos et al. have also suggested the formation of a short-range ordered C-A-S-H in limestone calcined clay cement (LC [3]) pastes, which converts into a long-range ordered C-A-S-H [28]. This precursor phase could be key regarding the longer setting time in cement formulations incorporating Al-containing SCMs and the reported lower efficacy of superplasticizers in these cements [29]. For instance, in LC [3] cement, a higher dosage of superplasticizers is required to ensure workability than in PC cement. This variation has been solely explained by clay particles absorbing water, effectively reducing the water-to-cement ratio and consequently leading to workability challenges [30]. However, the formation of this C-A-S-H precursor phase, which may have a high water content similar to that of the C-S-H globules [13,14], could also contribute to the loss of workability.

3.2. *Ex-situ analysis of the C-S-H and C-A-S-H precipitates*

To monitor structural changes in both C-A-S-H and C-S-H systems, we conducted ex-situ analyses of samples obtained throughout the reaction process. The final precipitates, collected after experiment completion were characterized using X-ray diffraction (XRD), ^{29}Si and ^{27}Al NMR spectroscopy, Fourier-transform infrared spectroscopy (FTIR),

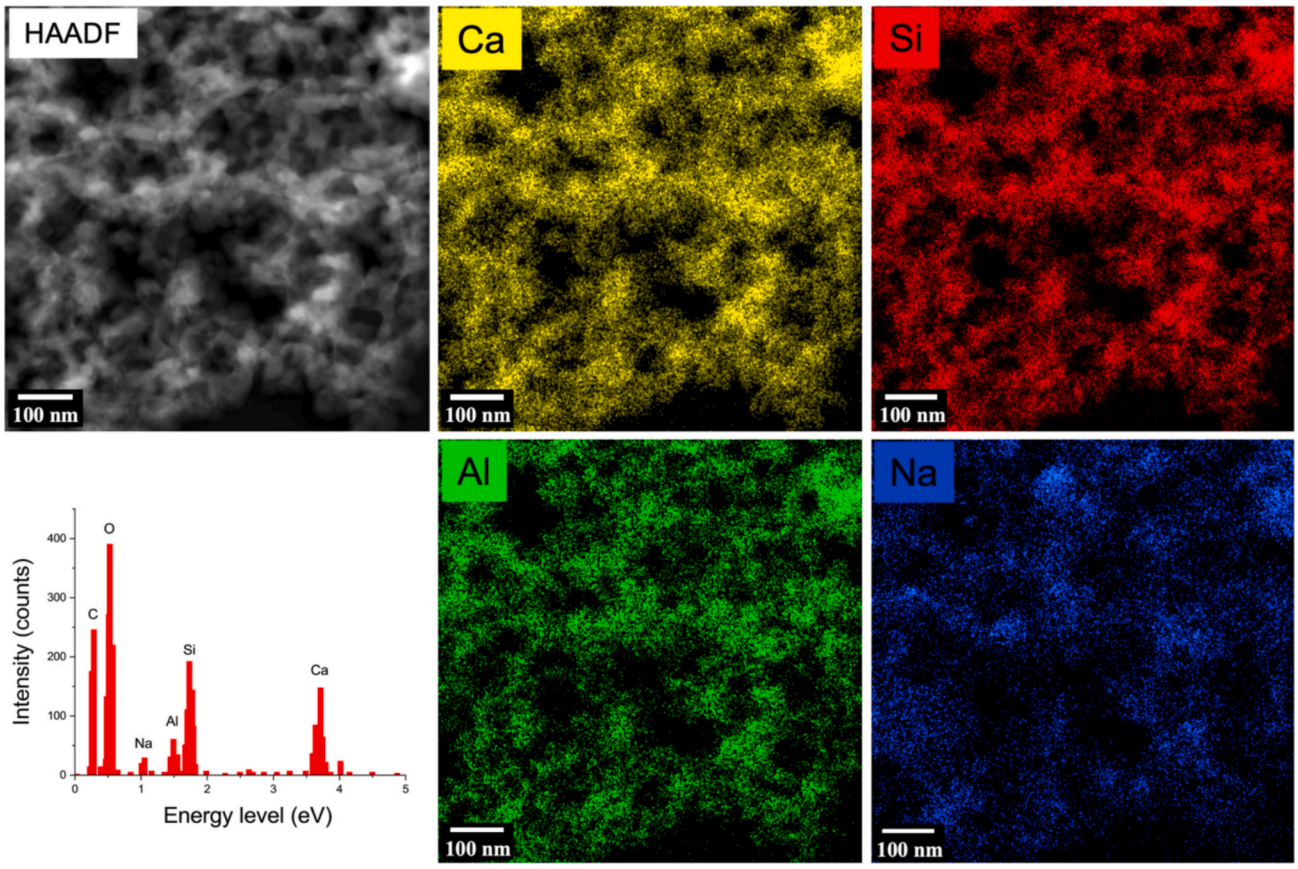

Fig. 5. TEM images of the C-A-S-H samples taken from an aliquot after 7000 s with corresponding EDX elemental mapping of Ca, Si, Al, and Na, as well as the overall EDX spectrum measured of the sample.

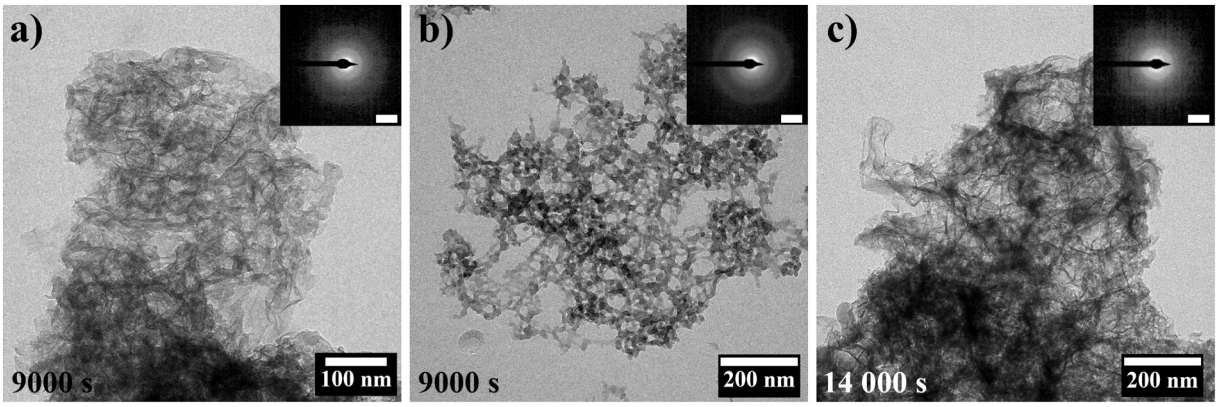

Fig. 6. TEM images of the C-A-S-H samples taken from aliquots after 9000 s and 14000 s, each with their corresponding SAED as an inset in the respective image. Scale of the SAED: 5 nm^{-1}.

and scanning electron microscopy (SEM) to evaluate differences in crystallinity, morphology, elemental composition, and thermal decomposition. Additionally, time-resolved aliquots were extracted at strategic transition points during the reaction: C-S-H at 5000 s (regime II), and C-A-S-H at 6000 s (regime II) and 8100 s (regime III), and analysed via XRD to track the evolution of their crystalline structure.

3.2.1. PXRD

The 16 h samples of both C-S-H (Fig. 7a) and C-A-S-H (Fig. 7b) depict a tobermorite-like structure [14] affected by nanocrystallinity and turbostratism [31]. No secondary phases such as katoite ($Ca_3Al_2(SiO_4)_3$-$Ca_3Al_2(OH)_{12}$) [32] or strätlingite ($Ca_4Al_2(OH)_{12}[AlSi(OH)_8]_2 \cdot 2H_2O$) [33] were formed during our experiments. Furthermore, the formation of $Ca(OH)_2$ phase was not observed, as Kumar et al. reported using also a titration approach [34]. In both samples, a series of peaks at approximately 7°, 17°, 29°, 32°, and 50° 2θ were identified as the characteristic peaks of C-S-H [31].

The XRD patterns were normalized to the highest intensity peak located at 29.4°. This peak in C-S-H and C-A-S-H patterns can be attributed to the (110) plane reflection (3.1 Å). In addition, a lower-intensity peak at 32.2° (or shoulder in the case of C-A-S-H) and a medium-intensity peak at 50° were observed in both materials. The peak at 32.2° corresponds to (200) plane reflection at 2.8 Å. The medium-intensity peak at 50° likely represents a (020) plane reflection at 1.8 Å

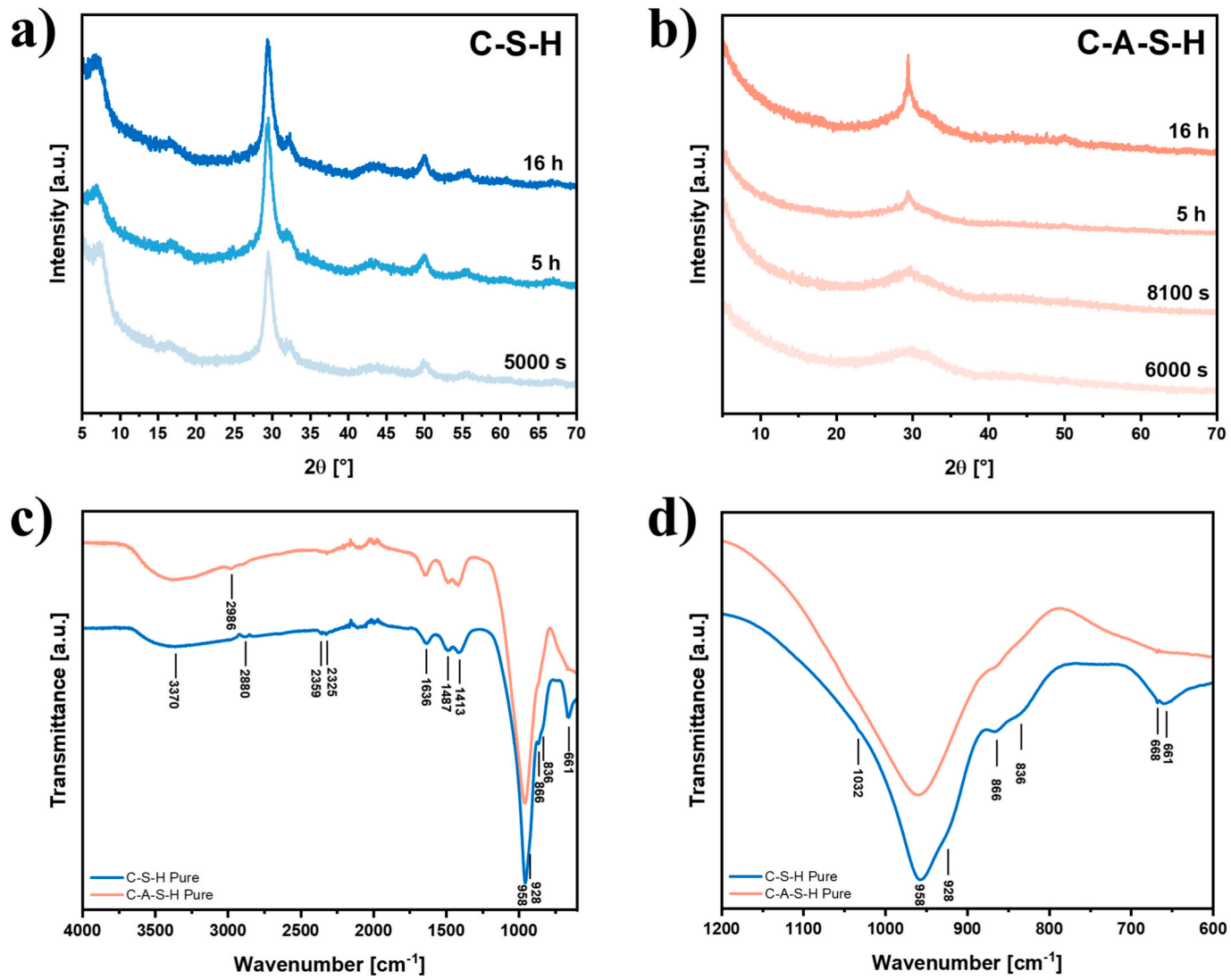

Fig. 7. Stacked PXRD measurements of filtered and dried a) C-S-H and b) C-A-S-H, each after different times during the titration. c) Stacked FTIR spectra of C-S-H and C-A-S-H in the range of 4000–600 cm^{-1}. d) Stacked FTIR pattern of the obtained C-S-H and C-A-S-H in the range of 1200–600 cm^{-1}.

[24]. Profile fittings conducted to calculate the full width at half maximum (FWHM) of the (110) reflection for C-S-H and C-A-S-H showed that C-S-H has a lower FWHM (1.12 ± 0.01°) than C-A-S-H (1.55 ± 0.02°), indicating that the incorporation of Al into the C-S-H matrix leads to a decreased crystallinity, which is in accordance with the literature [4]. The FWHM was obtained by a Gaussian fit using the Lavenberg Marquardt iteration algorithm.

The most notable difference between both materials after 16 h lies first in the lower intensity of the diffraction peaks in the case of C-A-S-H and secondly, in the presence of the 7.2° peak (d = 1.23 nm) in the C-S-H pattern, which is notably absent in the C-A-S-H pattern. This indicates that, unlike the C-S-H, the C-A-S-H crystallites are composed primarily of isolated layers or not stacked parallel. Previous studies have typically reported that incorporating Al into the C-S-H structure increases the interlayer spacing [35,36], yet in our observations, this peak completely disappeared. Yan et al., also observed a similar behaviour in C-S-H systems, noting a shift to a larger basal spacing at Ca/Si of 0.98 and complete disappearance at Ca/Si 0.75 [25]. The significantly shorter experimental duration and/or the presence of C-A-S-H globules still after 16 h might explain these discrepancies, as literature studies typically extend over weeks to months [37–39]. Extended reaction times of months or even years might therefore promote the development of regular interlayer spacing in the C-A-S-H precipitates [40].

3.2.1.1. Time-dependent evolution early stage. XRD analysis of samples drawn at different time points revealed distinct crystallization patterns between C-S-H and C-A-S-H systems at the early ages. At 5000 s (Fig. 7a), C-S-H already displayed well-defined peaks, including already discussed intense reflection at 29.5° and the characteristic low-angle reflection (basal spacing) at 7.4°, indicating rapid development of ordered structural arrangements post-nucleation.

In contrast, early C-A-S-H samples (6000 s and 8100 s) exhibited only a single, broad hump centered around 29.5° with lower intensity, characteristic of a poorly crystalline or amorphous phase (Fig. 7b). The similarity between these two time points indicated minimal structural evolution during regimes II and III. These broad XRD patterns, supported by our in-situ measurements and TEM observations, demonstrate that the aluminium-containing system undergoes gradual structural ordering from an initially amorphous phase to a more crystalline structure, as evidenced by the enhanced peak definition at 29.5° during extended aging (5 h and 16 h). A recent study investigating early-stage C-S-H formation demonstrated a crystallinity evolution pattern similar to our C-A-S-H system [16]. This parallel suggests that amorphous C-S-H likely forms in our system as well, but its transient nature prevented isolation and characterization of this intermediate phase.

3.2.2. FTIR

FTIR analyses were conducted mainly to investigate the differences in the interconnection of the silicate ions (Q^n). In the C-S-H system, the typical peaks previously reported were observed (Fig. 7d). In the lower region of the spectrum, around 655 cm^{-1}, a peak emerged related to Si—O—Si symmetric bending. The main peak, located approximately at 955 cm^{-1}, corresponds to the asymmetric stretching vibrations of Si—O generated by Q^2 units. Deconvolution analysis of the spectra revealed the complete list of peaks located at 998, 955, 914, 862, 852, 822, and 655 cm^{-1}. No Q [1]-related vibrations that should be located around 810 cm^{-1} were observed in our precipitates. The band at about 1630 cm^{-1} is related to H—O—H bending vibrations of molecular H_2O, and the broadband 2800–3700 cm^{-1} to O—H stretching vibrations (Fig. 7c). Slight and unavoidable carbonation of the precipitates was observed in the anti-symmetric stretching of CO_3^{2-} at approximately 1410 cm^{-1} and in the shoulder at 865 cm^{-1} due to the out-of-plane bending of CO_3^{2-}.

C-A-S-H shows a similar FTIR spectrum, with the Q^2 maximum peak centred at 960 cm^{-1}. This region, ranging from approximately 1200 cm^{-1} to 800 cm^{-1}, has broadened in the case of C-A-S-H compared with C-S-H, specifically from the 1200 to 960 cm^{-1} side of the peak. Another important difference is the water band at 2800–3700 cm^{-1} and 1645 cm^{-1}, which hints at higher water content in C-A-S-H compared with C-S-H. In addition, the carbonate bands are also more pronounced in the case of C-A-S-H. TGA corroborated both qualitative observations. Complex spectra of overlapping vibrations between 900 and 1030 cm^{-1}, including Al—O stretching, Si-O-Si, and Si-O-Al stretching vibrations, make it challenging to attribute specific vibrations accurately. In the vicinity of 670 cm^{-1}, vibrational modes related to tetrahedral four-membered rings Si-O-Si bending vibrations can be observed. Within the 750–900 cm^{-1} range, vibrations associated with the Al—O bond in AlO_4 units can be identified, confirming the presence of aluminium-oxygen bonds in the C-A-S-H framework. At 855 cm^{-1}, a peak corresponds to Al-O-H bonding. The appearance of a peak at approximately 880 cm^{-1} indicates the stretching vibration of a terminal Al-O-Si bond, suggesting interactions between aluminium and silicon in the C-A-S-H matrix. Within the 1034–1075 cm^{-1} range, peaks correspond to the symmetric bending of Al-O-H bonds. Finally, at 1420 cm^{-1}, a peak is linked to the stretching vibration of C—O bonds within carbonate groups in the C-A-S-H material.

3.2.3. NMR

Solid-state NMR spectroscopy was employed to examine Al coordination states (^{27}Al) and potential modifications to silicon environments (^{29}Si) in the 16 h C-S-H and C-A-S-H precipitates (Fig. 8). The analysis of ^{29}Si in C-S-H revealed characteristic silicate chain structures, with Q^1 and Q^2 environments as the dominant silicon species. The chemical shift of the main peak at −85 ppm indicates that Q^{2p} paired tetrahedra represents the primary silicon environment, although a high proportion of Q^1 sites (−79.5 ppm) was also observed. This silicon environment in C-S-H is well-documented in the literature and observed in phase-pure C-S-H prepared through the double decomposition of calcium salts and alkali silicates [15,16,34,41].

The ^{29}Si of the C-A-S-H precipitates revealed a significantly broader peak compared to C-S-H. A broad signal spanning from −68 ppm to −101 ppm indicates the presence of silicate units in various coordination environments, including Q^0, Q^1, Q^2, and Q^3. The predominant Q^{2p} species indicates a significant presence of chain-like structures, while the overall spectral broadening reflects increased structural disorder from aluminium incorporation. This spectral broadening aligns with observations by Sun et al. in synthetic C-A-S-H samples, demonstrating the slow structural evolution of C-A-S-H, as evident from their measurements at one week compared to our 16-hour time point [11]. Beyond the increased diversity of silicate Q^n species, this spectral broadening can be attributed to silicate species in pairing positions where each silicon tetrahedron bonds to another silicate tetrahedron and an Al(IV) tetrahedron ($Q^{2p,1Al(IV)}$), characterized by a chemical shift between −81 to −82 ppm [42,43].

Notably, broadening of the ^{29}Si NMR band is also characteristic of early-stage of synthetic C-S-H formation in the absence of Al [15,16,41]. In pure C-S-H systems, the initial amorphous globules, marked by a broad ^{29}Si NMR signal, transform into C-S-H foils within 1 h, accompanied by the development of well-defined Q^2 and Q^1 coordination peaks [16]. However, this transformation can be significantly delayed, extending to 24 h in the presence of PCEs [41] and up to 7 days in lower pH environments [15].

In our case, even if the final C-A-S-H precipitate after 16 h showed a foil-like appearance, albeit characterized by thinner morphologies, it seems that it is still composed by structurally disordered silicate environments similar to those observed in early-stage amorphous C-S-H, as evidenced by the broad ^{29}Si NMR signal. Zou et al. documented another precipitation synthesis of C-A-S-H that demonstrated increasingly broader signals in ^{29}Si NMR with increasing Al/Si ratios, extending into the Q^0 region at Al/Si ratios as low as 0.15 [44]. Their research draws an important connection between spectroscopic features and morphological characteristics, stating that the presence of Q^3 signal might be a reason for a globule-like morphology, a phenomenon. Notably, like our synthesis approach, they employed relatively short reaction times of 24 h.

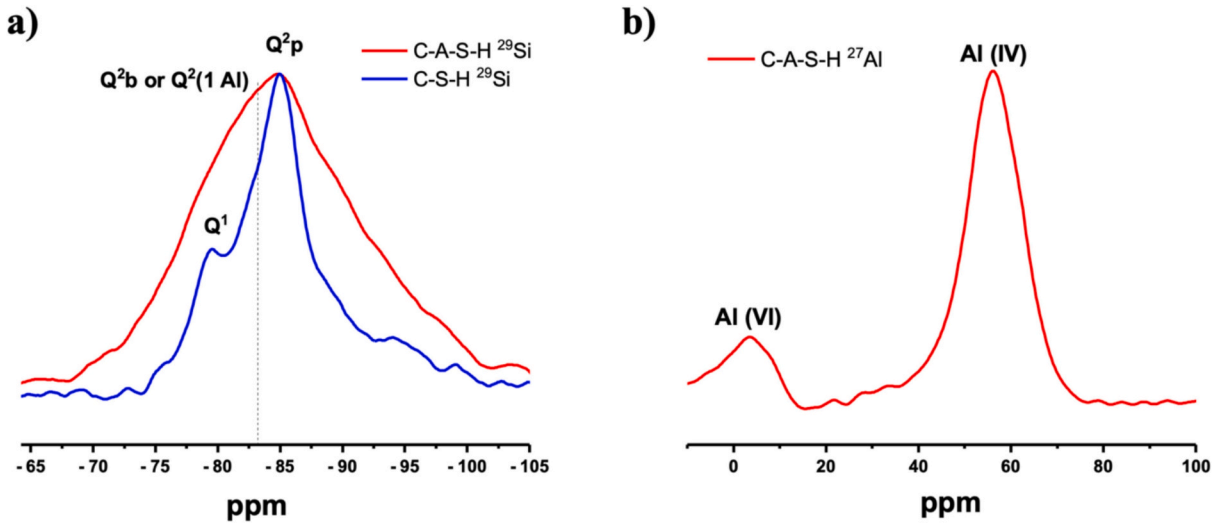

Fig. 8. a) ^{29}Si MAS NMR spectra of filtered and dried synthetic C-S-H and C-A-S-H and the corresponding b) ^{27}Al MAS NMR spectrum of C-A-S-H.

The ^{27}Al NMR spectrum demonstrates that aluminium in the C-A-S-H structure exists predominantly in tetrahedral coordination (Al(IV)), evidenced by the main peak at 56 ppm [36,45,46]. A small fraction of octahedrally coordinated aluminium (Al(VI)) is also present, indicated by a minor resonance at 3.25 ppm [11,46]. Combined with XRD analysis, these results confirm the absence of calcium aluminate hydrate (C_2AH_8) in our C-A-S-H precipitates [43]. While previous studies detected pentahedral coordinated aluminium (Al(V)) [10,11,36,47], this species was not observed in our C-A-S-H samples nor in recent XANES studies by Yan et al. on C-A-S-H samples synthesized in the presence of alkali hydroxide [26]. The factors controlling the presence or absence of Al(V) species in C-A-S-H remain elusive to the authors. While a detailed study of silicate and aluminate environment evolution over time would provide valuable insights into these structural transformations, such analysis constitutes an investigation by itself and is beyond the scope of this work.

3.2.4. TGA

Thermogravimetric analysis (TGA) was conducted on final C-S-H and C-A-S-H precipitates isolated by filtration after 16 h. The obtained TGA curves for both precipitates exhibited overlapping weight loss profiles, with a total weight loss of 21% for C-S-H and 24% for C-A-S-H, characterized by two distinct weight loss regions (Fig. SI-5). The initial weight loss from 25 °C to 300 °C is likely attributed to removing water molecules adsorbed or bound within the structure of C-S-H and C-A-S-H, as previously reported [48,49]. The derivative of the weight loss indicates that incorporating Al ions into C-A-S-H results in a higher amount of bounded water (larger area under the curve for C-A-S-H). The subsequent weight loss at temperatures between 300 °C and 550 °C, due to the dehydroxylation [50], is slightly higher for the case of C-A-S-H (3.6 wt%) compared to C-S-H (3 wt%). The final weight loss between 550 and 800 °C is related to the decomposition of carbonates present within the precipitates. As one could already anticipate from the FTIR, the C-A-S-H presents larger mass losses in this regime (1.4 wt%) than C-S-H (0.45 wt%) due to greater carbonation. TGA does not detect the decomposition of other aluminate phases or portlandite, which is consistent with FTIR and XRD results.

3.2.5. SEM

The SEM investigations of the C-S-H and C-A-S-H phases revealed morphological differences between both materials (Fig. 9). The superstructure of C-S-H is composed of closely packed sheets that are highly interconnected, creating a relatively dense three-dimensional network (Fig. 9a, b, and c). The morphological characteristics remained consistent across samples collected at different time points (5000 s, 5 h, and 16 h), corroborating our XRD and TEM findings regarding the rapid development of C-S-H sheet-like material in the C-S-H system. EDX-SEM analysis, after subtracting calcium bound in carbonates (quantified by TGA), revealed a Ca/Si ratio of 1.14 ± 0.07 (at.%) in the 16 h precipitates. Literature shows varying Ca/Si ratios for synthetic C-S-H, depending on pH or initial concentrations of the reactants [51,52]. However, for this initial investigation, we focused on a single stoichiometric condition with an initial Ca:Si ratio of 1:1, where both elements were added simultaneously to the reaction vessel at equal rates.

In contrast to C-S-H, the C-A-S-H system demonstrated a marked morphological transformation during its formation (Fig. 9d, e, f and g). The initial precipitates (6000 s and 8100 s) consisted of globular structures that progressively evolved into interconnected sheets during extended aging (5 h and 16 h). The mature C-A-S-H structure exhibited distinct characteristics from C-S-H, featuring higher porosity and finer texture. These noticeable morphological differences are most likely caused by incorporating Al in the material and the persistence of C-A-S-H globules that did not fully transform into foils during our experiments.

The compositional analysis of C-A-S-H precipitates after 16 h, corrected for calcium bound in carbonates (quantified by TGA), revealed Ca/Si and Al/Si ratios of 0.91 ± 0.03 and 0.24 ± 0.02, respectively in atomic %. Other comparable studies incorporating cations also report decreasing Ca/Si ratios [51], and that the microstructure of the C-A-S-H precipitates is affected by both the Ca/Si ratio and the Si/Al ratio [4]. In contrast to our studies, they demonstrated that the presence of Al promotes the formation of foils even at low Ca/Si ratios of 1. It is worth noticing that there were no noticeable differences between the precipitates obtained after 5 h and 16 h, highlighting the stability of both precipitates during this period. The Al/Si ratio of ~0.2 falls within the range commonly observed in various cementitious systems, from alkali-activated slags (AAS) [53,54], to slag-blended cement [55] and LC [3] systems [56].

4. Conclusion and outlook

In this study, the initial stages of the formation of C-S-H and C-A-S-H were investigated by monitoring the evolution of key physicochemical parameters of the solution under controlled synthetic conditions. Supersaturation was generated with respect to C-S-H and C-A-S-H,

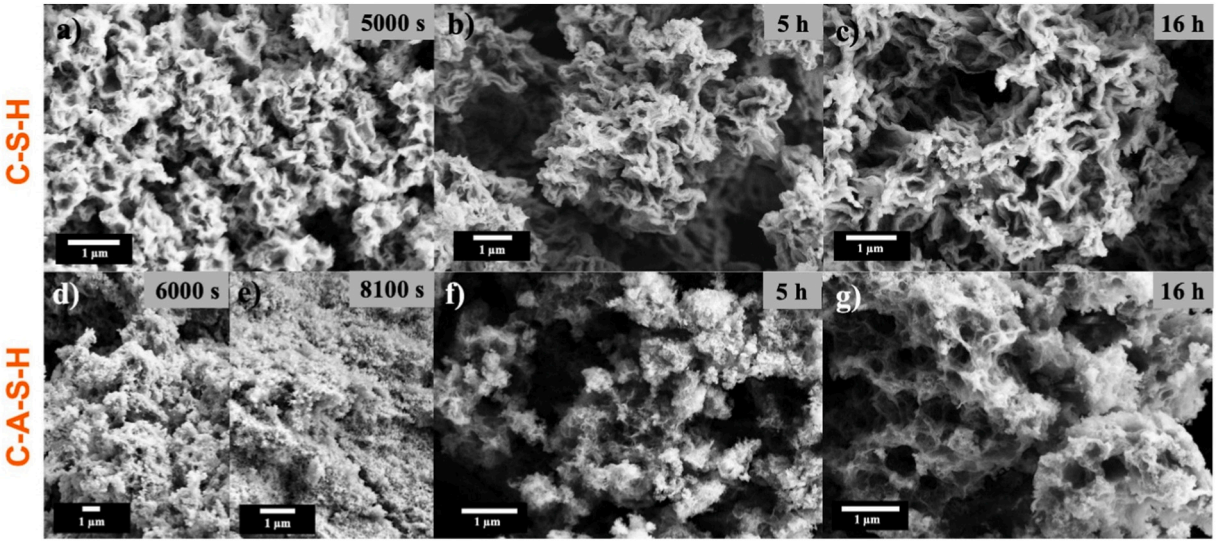

Fig. 9. SEM images of the filtered and dried precipitates from the C-S-H titration experiments after a) 5000 s, b) 5 h and c) 16 h, as well as SEM images of the synthetic C-A-S-H from the precipitation titration experiments after d) 6000 s, e) 8100 s, f) 5 h and g) 16 h.

respectively, by stepwise addition of stoichiometric calcium and silicon at a Ca/Al ratio of 0.2 to the reaction vessel, providing a highly reproducible crystallization scenario. The evolution of transmittance, conductivity, pH, and free Ca^{2+} concentrations enabled the identification of distinct differences in the initial crystallization stages of both phases. In the case of C-S-H, a single-step process was observed under the experimental conditions employed here. On the contrary, when Al was present in the crystallization media, the different probes revealed that the crystallization of C-A-S-H proceeded via a two-step process. The two distinct stages were repeatedly marked in the evolution of the solution's transmittance, free Ca^{2+}, and conductivity. Furthermore, aluminium's presence seems to promote calcium binding in the prenucleation stage, a topic currently under investigation using analytical ultracentrifugation (AUC).

Complementary TEM, XRD and SEM analyses confirmed the presence of a C-A-S-H precursor phase, as suspected by monitoring the evolution of the solution. Our results revealed the formation of an amorphous globular intermediate for C-A-S-H, which begins transforming in regime II (after approximately 7000 s) into thinner foil-like structures compared to the C-S-H precipitates. Unlike C-S-H, where the precursor species were not observed under our experimental conditions, most likely due to their rapid transformation, C-A-S-H exhibited an extended stability of its amorphous precursor phase. Furthermore, both final materials exhibited differences in their order at the atomic and nanometre scale: C-S-H precipitates exhibit a layered character with a basal spacing of 12.3 Å, whereas C-A-S-H crystallites appeared to be composed primarily of isolated layers or layers not stacked parallel to each other, as shown by the missing reflection of the interlayer spacing in the PXRD. Apart from the missing basal spacing, C-A-S-H was characterized by a lower crystallinity than C-S-H. The ^{29}Si NMR analysis revealed that C-A-S-H structure is dominated via Q^{2p} but exhibits significantly broader band compared to C-S-H, indicating diverse silicate coordination environments (Q^0 to Q^3) and increased structural disorder from aluminium incorporation. Aluminium (^{27}Al) exists predominantly in tetrahedral coordination (Al(IV)) with minor octahedral (Al(VI)) content, confirming the absence of calcium aluminate hydrate phases. Long-term investigations will provide insight into the transformation of both phases, and if C-A-S-H evolves to a more ordered material.

The synthetic formation of C-S-H and C-A-S-H in our study, although it might differ from the hydration processes in pure PC and blended systems incorporating Al-containing SCMs, allows us to isolate and understand fundamental crystallization mechanisms that are valuable across different cementitious systems. Our approach allows us to isolate and study specific aspects of hydrate formation without the compounding factors present in real cement systems. Identifying this precursor phase provides a potential means of controlling C-A-S-H formation. For instance, utilizing organic additives that interact specifically with the globules during C-A-S-H formation may prove an efficient method of controlling its formation. Our group's current research focuses on scaling up these experiments and isolating the globules to characterize them comprehensively. This effort complements the deeper characterization of the ion associates in regime I. The distinctive behaviour of C-A-S-H, particularly the persistence of a potentially more hydrated intermediate phase, may contribute to the loss of workability observed in blended cement containing aluminosilicate SCMs. Moreover, the stabilisation of C-A-S-H globules may be responsible for the retardation observed with the use of polycarboxylate ether superplasticisers, which may impede their transformation into sheet- or foil-like structures. These shortcomings could be addressed by identifying methods to reduce the lifespan of C-A-S-H globules and accelerate their transformation into foil-like structures. The results presented here represent a crucial initial step towards effectively addressing the challenges of Al-containing cements.

CRediT authorship contribution statement

Yannick H. Emminger: Writing – review & editing, Writing – original draft, Visualization, Investigation, Formal analysis, Conceptualization. **Luca Ladner:** Investigation, Formal analysis. **Cristina Ruiz-Agudo:** Writing – review & editing, Writing – original draft, Visualization, Investigation, Formal analysis, Conceptualization.

Declaration of competing interest

The authors declare that they have no affiliation with any organization with a direct or indirect financial interest in the discussed subject matter of this paper.

Acknowledgements

Cristina Ruiz Agudo expresses her gratitude to the *Zukunftskolleg* (*University of Konstanz*) and '*Dres. Edith and Klaus Dyckerhoff Foundation*' for their financial support for this project. Parts of this publication result from work carried out under Trans-National Access action under the support of EXCITE - EC- HORIZON 2020 - INFRAIA 2020 Integrating Activities for Starting Communities under grant agreement N. 101005611.

Appendix A. Supplementary data

Supplementary data to this article can be found online at https://doi.org/10.1016/j.cemconres.2025.107873.

Data availability

Data will be made available on request.

References

[1] M. Antoni, et al., Investigation of cement substitution by combined addition of calcined clays and limestone, in: 13th Int. Congr. Chem. Cem 6001, 2011, pp. 1–7.
[2] K.L. Scrivener, V.M. John, E.M. Gartner, Eco-efficient cements: potential economically viable solutions for a low-CO_2 cement-based materials industry, Cem. Concr. Res. 114 (2018) 2–26.
[3] R. Snellings, P. Suraneni, J. Skibsted, Future and emerging supplementary cementitious materials, Cem. Concr. Res. 171 (2023) 107199.
[4] E. Kapeluszna, Ł. Kotwica, A. Różycka, Ł. Gołek, Incorporation of Al in C-A-S-H gels with various Ca/Si and Al/Si ratio: microstructural and structural characteristics with DTA/TG, XRD, FTIR and TEM analysis, Constr. Build. Mater. 155 (2017) 643–653.
[5] B. Lothenbach, K. Scrivener, R.D. Hooton, Supplementary cementitious materials, Cem. Concr. Res. 41 (2011) 1244–1256.
[6] I.G. Richardson, G.W. Groves, Microstructure and microanalysis of hardened cement pastes involving ground granulated blast-furnace slag, J. Mater. Sci. 27 (1992) 6204–6212.
[7] C.A. Love, I.G. Richardson, A.R. Brough, Composition and structure of C–S–H in white Portland cement–20% metakaolin pastes hydrated at 25°C, Cem. Concr. Res. 37 (2007) 109–117.
[8] A.V. Girão, I.G. Richardson, R. Taylor, R.M.D. Brydson, Composition, morphology and nanostructure of C–S–H in 70% white Portland cement–30% fly ash blends hydrated at 55°C, Cem. Concr. Res. 40 (2010) 1350–1359.
[9] P. Faucon, et al., Aluminum incorporation in calcium silicate hydrates (C–S–H) depending on their Ca/Si ratio, J. Phys. Chem. B 103 (1999) 7796–7802.
[10] M.D. Andersen, H.J. Jakobsen, J. Skibsted, A new aluminium-hydrate species in hydrated Portland cements characterized by ^{27}Al and ^{29}Si MAS NMR spectroscopy, Cem. Concr. Res. 36 (2006) 3–17.
[11] G.K. Sun, J.F. Young, R.J. Kirkpatrick, The role of Al in C–S–H: NMR, XRD, and compositional results for precipitated samples, Cem. Concr. Res. 36 (2006) 18–29.
[12] R.J. Myers, S.A. Bernal, J.D. Gehman, J.S.J. Van Deventer, J.L. Provis, The role of Al in cross-linking of alkali-activated slag cements, J. Am. Ceram. Soc. 98 (2015) 996–1004.
[13] T. Sowoidnich, et al., The nucleation of C–S–H via prenucleation clusters, J. Chem. Phys. 158 (2023) 114309.
[14] N. Krautwurst, et al., Two-step nucleation process of calcium silicate hydrate, the nanobrick of cement, Chem. Mater. 30 (2018) 2895–2904.
[15] X. Shen, et al., Toward the formation mechanism of synthetic calcium silicate hydrate (C-S-H) - pH and kinetic considerations, Cem. Concr. Res. 172 (2023) 107248.

[16] X. Shen, et al., New insights into the non-classical nucleation of C-S-H, Cem. Concr. Res. 168 (2023) 107135.
[17] M. Schönlein, J. Plank, A TEM study on the very early crystallization of C-S-H in the presence of polycarboxylate superplasticizers: transformation from initial C-S-H globules to nanofoils, Cem. Concr. Res. 106 (2018) 33–39.
[18] M.R. Marsiske, et al., Immobilization of (aqueous) cations in low pH M-S-H cement, Appl. Sci. Switz. 11 (2021).
[19] A. Verch, D. Gebauer, M. Antonietti, H. Cölfen, How to control the scaling of $CaCO_3$: a 'fingerprinting technique' to classify additives, Phys. Chem. Chem. Phys. 13 (2011) 16811–16820.
[20] D. Gebauer, A. Völkel, H. Cölfen, Stable prenucleation calcium carbonate clusters, Science 322 (2008) 1819–1822.
[21] A. Picker, M. Kellermeier, J. Seto, D. Gebauer, H. Cölfen, The multiple effects of amino acids on the early stages of calcium carbonate crystallization, Z. Für Krist. - Cryst. Mater. 227 (2012) 744–757.
[22] A. Picker, L. Nicoleau, A. Nonat, C. Labbez, H. Cölfen, Influence of polymers on the nucleation of calcium silicate hydrates, Cem. Concr. Res. 174 (2023) 107329.
[23] B. Lothenbach, et al., Cemdata18: a chemical thermodynamic database for hydrated Portland cements and alkali-activated materials, Cem. Concr. Res. 115 (2019) 472–506.
[24] V. Kanchanason, J. Plank, Role of pH on the structure, composition and morphology of C-S-H–PCE nanocomposites and their effect on early strength development of Portland cement, Cem. Concr. Res. 102 (2017) 90–98.
[25] Y. Yan, et al., Effect of alkali hydroxide on calcium silicate hydrate (C-S-H), Cem. Concr. Res. 151 (2022) 106636.
[26] Y. Yan, et al., Al uptake in calcium silicate hydrate and the effect of alkali hydroxide, Cem. Concr. Res. 162 (2022) 106957.
[27] Z.Q. Tang, F.B. De Souza, R.J. Mulder, KwesiSagoe-Crentsil & Duan, W., Multistep nucleation and growth mechanism of aluminosilicate gel observed by cryo-electron microscopy, Cem. Concr. Res. 159 (2022) 106873.
[28] P.R. de Matos, et al., Effect of superplasticizer addition time and metakaolin source on the early-age hydration of limestone calcined clay cement (LC^3), Mater. Struct. - Revis. 2022 (2022) 0123456789.
[29] R. Hay, K. Celik, Effects of water-to-binder ratios (w/b) and superplasticizer on physicochemical, microstructural, and mechanical evolution of limestone calcined clay cement (LC^3), Constr. Build. Mater. 391 (2023) 131529.
[30] N. Nair, K. Mohammed Haneefa, M. Santhanam, R. Gettu, A study on fresh properties of limestone calcined clay blended cementitious systems, Constr. Build. Mater. 254 (2020) 119326.
[31] S. Grangeon, et al., Structure of nanocrystalline calcium silicate hydrates: insights from X-ray diffraction, synchrotron X-ray absorption and nuclear magnetic resonance, J. Appl. Crystallogr. 49 (2016) 771–783.
[32] E. Passaglia, R. Rinaldi, Katoite, a new member of the $Ca_3Al_2(SiO_4)_3$-$Ca_3Al_2(OH)_{12}$ series and a new nomenclature for the hydrogrossular group of minerals, Bull. Mineral. 107 (1984) 605–618.
[33] I. Santacruz, et al., Structure of stratlingite and effect of hydration methodology on microstructure, Adv. Cem. Res. 28 (2016) 13–22.
[34] A. Kumar, et al., The atomic-level structure of cementitious calcium silicate hydrate, J. Phys. Chem. C 121 (2017) 17188–17196.
[35] G. Renaudin, J. Russias, F. Leroux, F. Frizon, C. Cau-dit-Coumes, Structural characterization of C–S–H and C–A–S–H samples—part I: long-range order investigated by Rietveld analyses, J. Solid State Chem. 182 (2009) 3312–3319.
[36] E. L'Hôpital, B. Lothenbach, D.A. Kulik, K. Scrivener, Influence of calcium to silica ratio on aluminium uptake in calcium silicate hydrate, Cem. Concr. Res. 85 (2016) 111–121.
[37] Raúl Fernández, A.I. Ruiz, J. Cuevas, Formation of C-A-S-H phases from the interaction between concrete or cement and bentonite, Clay Miner. 51 (2016) 223–235.
[38] F. Avet, E. Boehm-Courjault, K. Scrivener, Investigation of C-A-S-H composition, morphology and density in limestone calcined clay cement (LC^3), Cem. Concr. Res. 115 (2019) 70–79.
[39] Z. Dai, T.T. Tran, J. Skibsted, Aluminum incorporation in the C-S-H phase of white Portland cement-metakaolin blends studied by ^{27}Al and ^{29}Si MAS NMR spectroscopy, J. Am. Ceram. Soc. 97 (2014) 2662–2671.
[40] E. L'Hôpital, B. Lothenbach, G. Le Saout, D. Kulik, K. Scrivener, Incorporation of aluminium in calcium-silicate-hydrates, Cem. Concr. Res. 75 (2015) 91–103.
[41] J. Plank, M. Schönlein, V. Kanchanason, Study on the early crystallization of calcium silicate hydrate (C-S-H) in the presence of polycarboxylate superplasticizers, J. Organomet. Chem. 869 (2018) 227–232.
[42] M.D. Andersen, H.J. Jakobsen, J. Skibsted, Incorporation of aluminum in the calcium silicate hydrate (C−S−H) of hydrated Portland cements: a high-field ^{27}Al and ^{29}Si MAS NMR investigation, Inorg. Chem. 42 (2003) 2280–2287.
[43] A. Kunhi Mohamed, et al., The atomic-level structure of cementitious calcium aluminate silicate hydrate, J. Am. Chem. Soc. 142 (2020) 11060–11071.
[44] F. Zou, M. Zhang, C. Hu, F. Wang, S. Hu, Novel C-A-S-H/PCE nanocomposites: design, characterization and the effect on cement hydration, Chem. Eng. J. 412 (2021) 128569.
[45] S. Komarneni, et al., ^{27}Al and ^{29}Si magic angle spinning nuclear magnetic resonance spectroscopy of Al-substituted tobermorites, J. Mater. Sci. 20 (1985) 4209–4214.
[46] G. Renaudin, J. Russias, F. Leroux, C. Cau-dit-Coumes, F. Frizon, Structural characterization of C–S–H and C–A–S–H samples—part II: local environment investigated by spectroscopic analyses, J. Solid State Chem. 182 (2009) 3320–3329.
[47] X. Pardal, F. Brunet, T. Charpentier, I. Pochard, A. Nonat, ^{27}Al and ^{29}Si solid-state NMR characterization of calcium-aluminosilicate-hydrate, Inorg. Chem. 51 (2012) 1827–1836.
[48] B. Lothenbach, G. Le Saout, E. Gallucci, K. Scrivener, Influence of limestone on the hydration of Portland cements, Cem. Concr. Res. 38 (2008) 848–860.
[49] B. Lothenbach, F. Winnefeld, Thermodynamic modelling of the hydration of Portland cement, Cem. Concr. Res. 36 (2006) 209–226.
[50] J. Środoń, Identification and quantitative analysis of clay minerals, in: Developments in Clay Science Vol. 5, Elsevier, 2013, pp. 25–49.
[51] J. Siramanont, B.J. Walder, L. Emsley, P. Bowen, Iron incorporation in synthetic precipitated calcium silicate hydrates, Cem. Concr. Res. 142 (2021) 106365.
[52] M. Harris, G. Simpson, K. Scrivener, P. Bowen, A method for the reliable and reproducible precipitation of phase pure high Ca/Si ratio (>1.5) synthetic calcium silicate hydrates (C S H), Cem. Concr. Res. 151 (2022) 106623.
[53] S.-D. Wang, K.L. Scrivener, ^{29}Si and ^{27}Al NMR study of alkali-activated slag, Cem. Concr. Res. 33 (2003) 769–774.
[54] G. Le Saoût, M. Ben Haha, F. Winnefeld, B. Lothenbach, Hydration degree of alkali-activated slags: a ^{29}Si NMR study, J. Am. Ceram. Soc. 94 (2011) 4541–4547.
[55] I.G. Richardson, The nature of C-S-H in hardened cements, Cem. Concr. Res. 29 (1999) 1131–1147.
[56] F. Avet, X. Li, K. Scrivener, Determination of the amount of reacted metakaolin in calcined clay blends, Cem. Concr. Res. 106 (2018) 40–48.